International Journal of Heat and Mass Transfer 139 (2019) 58–68

Contents lists available at ScienceDirect

International Journal of Heat and Mass Transfer

journal homepage: www.elsevier.com/locate/ijhmt

Two-phase flow and oxygen transport in the perforated gas diffusion layer of proton exchange membrane fuel cell

Zhiqiang Niu [a,b], Jingtian Wu [b], Zhiming Bao [a], Yun Wang [b,*], Yan Yin [a], Kui Jiao [a,*]

[a] State Key Laboratory of Engines, Tianjin University, 135 Yaguan Rd, Tianjin 300350, China
[b] Renewable Energy Resources Laboratory (RERL), Department of Mechanical and Aerospace Engineering, University of California, Irvine, CA 92697-3975, United States

ARTICLE INFO

Article history:
Received 17 January 2019
Received in revised form 7 April 2019
Accepted 5 May 2019

Keywords:
Perforation
Wettability
Oxygen diffusion
Volume of fluid
Gas diffusion layer

ABSTRACT

Liquid water transport in perforated gas diffusion layers (GDLs) is numerically investigated using a three-dimensional (3D) two-phase volume of fluid (VOF) model and a stochastic reconstruction model of GDL microstructures. Different perforation depths and diameters are investigated, in comparison with the GDL without perforation. It is found that perforation can considerably reduce the liquid water level inside a GDL. The perforation diameter (D = 100 μm) and the depth (H = 100 μm) show pronounced effect. In addition, two different perforation locations, i.e. the GDL center and the liquid water break-through point, are investigated. Results show that the latter perforation location works more efficiently. Moreover, the perforation perimeter wettability is studied, and it is found that a hydrophilic region around the perforation further reduces the water saturation. Finally, the oxygen transport in the partially-saturated GDL is studied using an oxygen diffusion model. Results indicate that perforation reduces the oxygen diffusion resistance in GDLs and improves the oxygen concentration at the GDL bottom up to 101% (D = 100 μm and H = 100 μm).

1. Introduction

Polymer electrolyte membrane fuel cells (PEMFCs) have great potential to offer power sources for the automotive vehicles owing to their distinct merits such as high energy conversion efficiency, quick start-up capability and so on [1,2]. The gas diffusion layer (GDL) is vital in the water management of PEMFCs [3]. The presence of excessive liquid water in the cathode GDL will cause "water flooding" and block the reactant transport to catalyst sites [4]. Therefore, it is critical to improve water management in the GDL to enhance cell performance [5].

Generally, GDL consists of insufficiently hydrophobic porous substrates such as carbon paper or carbon cloth [6]. As well known, the transport of liquid water in the GDL mainly depends on microstructures and hydrophobicity of pores [5]. Various approaches have been adopted to optimize or modify the porous structures of the GDL for efficient water removal, such as addition of microporous layer (MPL) [7–10], polytetrafluoroethylene (PTFE) treatment [11–13] and usage of metal porous materials [14,15]. Shan et al. [9] experimentally investigated the performance of GDL with/without MPL at different humidification conditions via a segmented cell technique. They found MPL can improve the cell performance under both high and low humidification because of its dense pore structures. Giorgi et al. [13] investigated the effects of different PTFE contents on the performance of low Pt loading PEMFC. They found adding PTFE mitigates the electrode flooding and improves the cell performance. They found addition of PTFE can avoid the electrode flooding and improve the cell performance. Choi et al. [15] proposed Ti foam as an alternative GDL for PEMFCs. Their experimental data indicated that Ti foam can provide better reliability and chemical stability than traditional Toray carbon paper. Further optimization on the GDL structures is still necessary to improve the performance of PEMFCs.

Recently, the perforation in GDLs has attracted considerable attentions because the artificially created pathways can effectively change liquid water distribution in GDLs [16–20]. Gerteisen et al. [16] firstly modified the GDL by laser-perforation and conducted in-situ experiments to test PEMFC with new GDL structures. The experimental data shows a better dynamic and overall performance is obtained by the perforated GDL. Subsequently, the cathode GDLs with perforation are investigated continually by a PEM fuel cell stack in Gerteisen's further work [17]. They found that the perforation improves the water transport in the GDL as well as cell stability if the stack in medium and high current density range. However, above researches mainly focus on the effects of perforation on the overall cell performance, detailed liquid water

* Corresponding authors.
E-mail addresses: yunw@uci.edu (Y. Wang), kjiao@tju.edu.cn (K. Jiao).

https://doi.org/10.1016/j.ijheatmasstransfer.2019.05.008
0017-9310/

behaviors in the pore structures of perforated GDLs are still not clear.

Several visualization techniques have been employed to investigate the liquid water distribution in perforated GDLs such as neutron radiography [21–23], environmental scanning electron microscope (ESEM) [24,25] and synchrotron X-ray radiography [26–30]. Lu et al. [21] employed high resolution neutron radiography to visualize the liquid water distribution in GDLs with laser perforation. They found that the perforated GDL can significantly reduce water transport resistance and enhance liquid water breakthrough in GDLs. Alink et al. [24] adopted environmental scanning electron microscope (ESEM) to investigate the liquid water behaviors in the ex-situ GDL. They found the lower liquid water saturation in the perforated GDL and larger in-plane water transport towards the perforations. In their further work [27], the influence of laser perforation of the GDL on the in-situ performance of PEMFC was investigated by combining synchrotron radiography and ESEM techniques. Their results reveal that laser perforation can form hydrophilic regions because of PTFE loss and improve the cell performance at dry conditions. However, these imaging techniques are usually costly and time consuming.

As in other technological branches, numerical simulations are expected to help understand the complex liquid water behaviors in GDLs via various multiphase models such as the multiphase mixture (M^2) model [31–35], Lattice Boltzmann (LB) model [36–39], pore network (PN) model [40–42] and volume of fluid (VOF) model [43–48]. Wang and Chen [31] employed a M^2 model to elucidate water distribution in the through-plane (TP) direction of the GDL and validate their results with high-resolution neutron imaging data. Fang et al. [36] developed a two-phase LBM model to simulate water distributions in perforated GDLs and the effective transport properties in the partially-saturated GDLs. Their results revealed that the perforation can significantly affect the water transport in hydrophobic GDLs. Carrere and Part [42] presented a PN model to simulate the pore filling process of liquid water in the operating cathode GDL. Their model associates the water management and cell performance and provides different method to understand liquid water behaviors in the GDL. Niu et al. [45] adopted a two-phase VOF model to study the liquid water cross flow under ribs and they developed a diagram to illustrate the possible liquid water flow paths. Niu et al. [46–48] further extended their VOF study and GDL reconstruction model to investigate the TP water distributions by accounting for the different spatial porosity distribution and mixed wettability in the GDL. Good agreement was achieved for the local liquid water profile under low pressure, along with the liquid saturation-capillary pressure correlation for the GDLs with different PTFE loadings.

Though many numerical works have been performed to study the air-water flow in GDLs, few pay attention to the liquid water behaviors and oxygen diffusion in the microstructures of perforated GDLs [36]. In this study, a two-phase VOF model and a stochastic GDL reconstruction model are adopted to investigate the effects of dimensional parameters of perforation, such as the depth H, diameter D and location of perforation, on the liquid water dynamics and distributions in the pores of GDLs, as shown in Fig. 1a. Moreover, the impacts of the perforation perimeter wettability and oxygen diffusion are also investigated.

2. Methodology

2.1. Volume of fluid model

The volume of fluid (VOF) model is appropriate to capture the interface between two immiscible fluids by resolving the advection of phase volume fraction γ. The volume fraction γ takes the value 1 if the cell is occupied by liquid phase and value 0 for gas phase. The cells with γ ranging from 1 to 0 refer the two-phase interface. The governing equations for the two-phase VOF model in this study are listed as follows [45–47]:

Continuity equation:

$$\nabla \cdot \vec{U} = 0 \tag{1}$$

where ∇ is Nabla operator which denotes vector differential operator, the operator "$\cdot$" denotes the inner product of two tensors. i.e. the "$\nabla\cdot$" denotes the divergence. $\vec{U}$ is the effective velocity vector shared by the two phases throughout the flow domain, which is defined as

$$\vec{U} = \gamma \vec{U}_l + (1-\gamma)\vec{U}_g \tag{2}$$

Phase conservation equation:

$$\frac{\partial \gamma}{\partial t} + \nabla \cdot \left(\vec{U}\gamma\right) + \nabla \cdot \left[\vec{U}_r \gamma(1-\gamma)\right] = 0 \tag{3}$$

where t is the time, $\vec{U}_r = \vec{U}_l - \vec{U}_g$ is the relative velocity of liquid and gas at the interface, designated as "compression velocity", the subscript r here denotes "relative velocity". The subscripts l and g denote the liquid phase and gas phase respectively.

Momentum equation:

$$\frac{\partial\left(\rho\vec{U}\right)}{\partial t} + \nabla \cdot \left(\rho \vec{U}\vec{U}\right) - \nabla \cdot \left(\mu \nabla \vec{U}\right) - \left(\nabla \vec{U}\right) \cdot \nabla \mu = -\nabla p_d - \vec{g} \cdot \vec{x} \nabla \rho + f_s \tag{4}$$

where $\vec{x}$ is the position vector and $\vec{g}$ is the gravity vector, the subscript d denotes "dynamic". f_s refers a volumetric force source. The fluid properties in Eq. (4), such as density ρ and viscosity μ, are updated according to the γ, namely as:

$$\rho = \gamma \rho_l + (1-\gamma)\rho_g \tag{5}$$

$$\mu = \gamma \mu_l + (1-\gamma)\mu_g \tag{6}$$

p_d is a modified pressure for simplifying the boundary conditions, defined as

$$p_d = p - \rho \vec{g} \cdot \vec{x} \tag{7}$$

In this VOF model, the continuum surface force (CSF) model is adopted to account for the effects of surface tension at the liquid-gas interface by adding a volumetric force source f_s to Eq. (4) as

$$f_s = \sigma \kappa \nabla \gamma \tag{8}$$

where σ is the surface tension coefficient between water and air, and the subscript s denotes "surface tension", κ is the curvature of two-phase interface and is approximated as the divergence of unit interface normal $\vec{n}$, i.e.

$$\kappa = -\nabla \cdot \vec{n} = -\nabla \cdot \left(\frac{\nabla \gamma}{|\nabla \gamma|}\right) \tag{9}$$

The wettability of wall is accounted for by adjusting the surface unit normal $\vec{n}$ in the cells adjacent to the wall according to the following equation:

$$\vec{n} = \vec{n}_w \cos\theta + \vec{t}_w \sin\theta \tag{10}$$

where $\vec{n}_w$ is the unit vector normal to the wall, $\vec{t}_w$ is the unit vector tangential to the wall, the subscript w denotes wall. θ is the contact angle. In this study, the constant contact angle is considered. Based on the Young-Laplace equation, the capillary pressure P_c, defined as the difference of liquid pressure P_l and gas pressure P_g

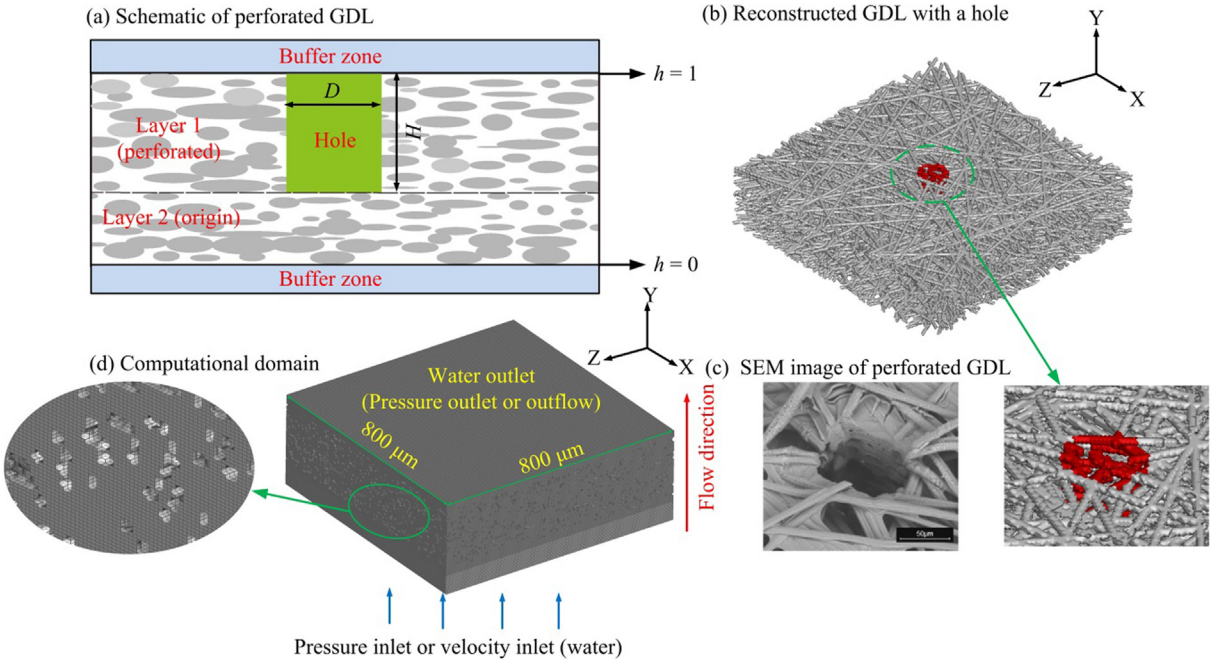

Fig. 1. Schematics of (a) dual GDL design with perforation, (b) reconstructed fiber structures with perforation, (c) scan electron microscope (SEM) images of laser-perforated GDL [16].

in porous media, is related to the average pore radius r and the contact angle θ of the pore surface:

$$P_c = P_l - P_g = -\frac{2\sigma\cos\theta}{r} \tag{11}$$

2.2. Oxygen diffusion model

In a partially-saturated GDL, the local oxygen concentration C is governed by the diffusion equation [47]:

$$\nabla \cdot (D\nabla(C)) = 0 \tag{12}$$

where D is the oxygen diffusion coefficient. At the phase interface between air and liquid water, the concentration equilibrium is characterized by Henry law:

$$He = \frac{C_g}{C_l} \tag{13}$$

where He is constant Henry coefficient, and a value of 42.785 was chosen [47]. To consider the oxygen transport in both air and water conveniently, a scalar C_e named as effective concentration is introduced [47]:

$$C_e = \begin{cases} C & \text{inside the gas phase} \\ CHe & \text{inside the liquid phase} \end{cases} \tag{14}$$

The final governing equation for C_e is written as:

$$\nabla \cdot (D_e \nabla C_e) = 0 \tag{15}$$

where D_e is the effective diffusion coefficient which written as [47]:

$$D_e = \left[\gamma\left(\frac{D_l}{He}\right)^{-1} + (1-\gamma)\left(\frac{D_g}{1}\right)^{-1}\right]^{-1} \tag{16}$$

where γ is the water phase fraction defined in VOF model, D_l and D_g are the oxygen diffusion coefficient in the liquid and gas phase, respectively. Here, the D_l and D_g are $1.97 \times 10^{-9}\ m^2\ s^{-1}$ and $2.19 \times 10^{-5}\ m^2\ s^{-1}$, respectively [47]. Under dry condition, the water phase fraction γ is zero and all the diffusivity is set to D_g.

2.3. Reconstruction of GDLs and perforated GDLs

The carbon paper GDL usually consists of randomly distributed carbon fibers. The GDL is assumed as a stack of fibers and reconstructed by using the stochastic method in our previous studies [45–48], which is popular in the reconstruction of GDL [6,36,37,39,43,44]. The fiber diameter is 8 μm, consistent with experimental measurement [49]. TGP-H-060 is reconstructed in Section 3.1 for experimental validation [50]. For the perforated GDLs in Section 3.2–3.5, a no-perforation GDL is first reconstructed with an average porosity of 0.73, which excludes the effect of varying porosity in the TGP-H-060. The perforation hole is achieved by removing the fibers within a cylindrical region, as shown in Fig. 1a. The perforation perimeter locates in the region 20 μm from the surface of perforation. The fiber surface in this region can set as hydrophobic or hydrophilic to investigate the effect of wettability. The microstructures of perforated GDL with a perforation diameter D = 50 μm are shown in Fig. 1b and compared with scanning electron microscope (SEM) image [16]. As a fundamental study, we only consider one perforation in the GDL.

2.4. Initial and boundary conditions

(a) Two-phase VOF model

The perforated GDL samples in this study are 192 μm thick with a cross-section of 800 μm × 800 μm. In Section 3.1, for model validation the water saturation s is obtained by performing a water-invasion process and compared with ex-situ experiment, where a constant pressure difference 1000 Pa was imposed on the two sides of the GDL. In the operation of PEMFC, liquid water is produced from the cathode and removed via the GDL, thus, a water flow rate, i.e. water velocity inlet is suitable to study water removal in PEMFC. Therefore, in the Section 3.2–3.5, a constant water velocity of 0.005 m s^{-1} is set to drive water flow. This water velocity corresponds to the water production rate of fuel cell at a current density of 2500 A cm^{-2} (normal PEM fuel cell operates up to about 2 A cm^{-2}). For the predicted water velocity larger than normal fuel

cell water production rate, we think two points are important to justify using this value: (1) Water in the cathode GDL may come from other resources, including the anode side via water electroosmosis, water addition or condensation from neighboring area, and water accumulation (or local storage). Water accumulation (or storage) has been observed by other experiments, which leads to periodic liquid break-through GDL [51,52]. And (2) It is also of fundamental importance to investigate general two-phase flows in carbon papers.

It is noted a buffer zone (thickness 20 μm) is placed on the top of GDL zone. An interior boundary is set for the interface between the GDL and buffer zone. And the top of the buffer zone is set as outflow to allow liquid and gas flow out. In this study, the details of gas flow in the flow channel are not specified to better focus on the internal two-phase flow in the microstructures of GDL. This simplification has been widely accepted in the two-phase models of reconstructed GDLs [36,39,43–48,53,54]. In practical PEMFC operation, a number of perforations are usually manufactured in the GDL under the flow channel. In addition, in the literature the periodic [36,39], symmetry [44] and no-slip boundary conditions [43,53] have been proposed for the GDL. We compared the symmetry and no-slip boundary conditions in our simulation, and found almost the same predictions. In addition, because of the asymmetry in GDL it is preferred to adopt the no-slip boundary at the GDL sides for large GDL samples [54]. The size of present study (the cross section 800 μm × 800 μm) is nearly four times of previous studies and large enough to exclude the effects of the GDL sides [36,39,43,44].

The PTFE is usually employed to treat GDLs to render the fibers hydrophobic, and the spatial PTFE distribution may result in the mixed wettability of the GDL [48,55]. The present study focuses on the effect of perforation, and the spatial PTFE distribution is not in this scope. Thus, the fiber surface, due to PTFE treatment, is set hydrophobic with a constant contact angle $\theta = 109°$. For the perforation perimeter in Section 3.5, 80° for the hydrophilic fiber surface [48].

Initially, there was no water in GDLs. The capillary pressure hysteresis is observed in the drainage (gas intrusion) and imbibition (liquid intrusion) processes because of the contact angle hysteresis [56,57]. In this study, only liquid water intrusion is studied. In addition, the assumption of constant contact angle has been widely used to study two-phase flows in GDLs [35–48,53,54,56].

(b) Oxygen diffusion model

To obtain the oxygen concentration distribution in the partially-saturated GDL, the 3D water distribution predicted by the VOF model was used as input for computation. The Dirichlet (oxygen concentration 50 mol m^{-3}) and Neumann (oxygen flux −500 mol m^{-2}) boundary conditions are imposed at the top and bottom of the GDL respectively, while the others are treated as walls.

2.5. Numerical procedures

In the present model, the computational domains of the perforated GDL samples are discretized with 9 million hexahedral cells (267 × 131 × 267 in the GDL for the x, y and z dimensions, respectively), as shown in Fig. 1d. The open source software Open FOAM is employed to perform all the simulations. The pressure-implicit with splitting of operators (PISO) is employed to solve the two-phase VOF governing equations. The adaptive time step is adopted to guarantee the Courant number no more than 1. The convection, Laplacian and gradient terms in the flow and volume fraction governing equations are discretized using a second-order scheme, and the time term is discretized using a first-order scheme. The parallelization of OpenFOAM is performed by message passing interface (MPI) and is generally linked to open source MPI (Open MPI) library. Open MPI integrates technologies and resources from different projects and can significantly improve its scalability, performance of parallel computation. All the simulations in this study were carried out in the Tianhe-HPC1 system at the National Supercomputer center in China. Each case was conducted for a time period of 50 ms until the steady flow was reached, which took about 21,504 CPU hours using 112 Intel Xeon @2.93 GHz processors in parallel.

3. Results and discussion

3.1. Model validation

The local porosity and liquid water saturation of the reconstructed Toray carbon paper (TGP-H-060) in the through-plane (TP) direction are validated with X-ray tomographic experiment data [50], see Fig. 2. The dimensions and boundary conditions of the computational domain are same as those shown in Fig. 1d. It is noted that the boundary settings in this section is different from those in Section 3.2–3.5. In this study, a pressure difference is employed at two sides of the computational domain, which is consistent with experiment [50]. It is seen that the predicted results agree reasonably well with X-ray experimental data. Validation of the capillary pressure versus liquid water saturation was conducted in our previous study [46]. In this and following sections, the local porosity and saturation were calculated by averaging in the in-plane dimension. The relative thickness h is defined as the dimensionless thickness (i.e. $h = 0$ at the GDL bottom and $h = 1$ at the GDL top), see Fig. 1a.

3.2. Effects of the layer thickness, H

Perforated GDLs are usually penetrated by laser beam [16,17]. The penetrated perforation in the GDL will reduce the electrical

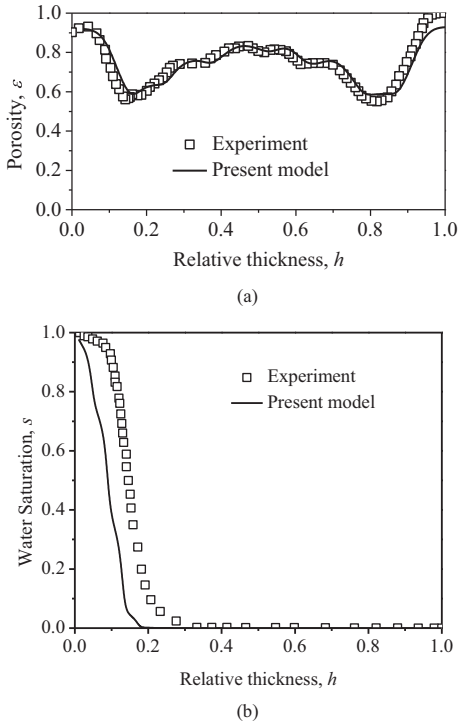

Fig. 2. Comparison of the liquid water saturations and porosity in the TP direction of Toray-H-060 carbon paper between the present results and X-ray experiment data [50]. Operating conditions: the fiber contact angle $\theta = 109°$ and $\Delta p = 1000$ Pa.

conductivity by reducing the volume of solid fiber and contact area with micro porous layer or catalyst layer. In this study, a dual layer design is adopted to reduce this negative effect, as shown in Fig. 1a. The top layer can be treated with laser perforation and the bottom layer keeps origin. In this way, the depth of perforation H can be adjusted and optimized. In this study, there is only one perforation in the GDL. Three perforation depths, H = 50 μm, 100 μm, and 150 μm are investigated and compared with the GDL without perforation. The perforation is located at X = 500 μm and Z = 700 μm, which is fairly close to the one of liquid water break-through points in the GDL without perforation. The liquid water break-through points are the locations where liquid water emerges out of the GDL. In the GDL without perforation, these points are highlighted in the Fig. 3. We chose one of them (X = 500 μm and Z = 700 μm) as a reference in this study.

Fig. 4 shows the local porosities ε and local liquid water saturation s in the TP direction for different perforation depths H. The local water saturation s refers the one averaged in the in-plane (IP) direction. It is seen thast the small depth H = 50 μm decreases the liquid water slightly. This is because this depth has not reached the liquid water front, see Fig. 5. When perforation depth increases to 100 μm, the perforation reaches the liquid water front and significantly decreases the local liquid water in the GDL. As perforation depth further increases to 150 μm, the liquid water has little decrement compared with H = 100 μm. This is because the perforation has reached a "flooding region" where the perforation takes few effects. Thus, a perforation depth 100 μm is suitable for the GDL in this study. It is also observed that the liquid water saturation profiles are different from those in Fig. 2b. This is caused by the pressure difference boundary set in Fig. 2b. The pressure difference (1000 Pa) is smaller than the liquid break-through capillary pressure of TGP-H-060 (about 5000 Pa) [50], thus liquid water fails to break through the GDL and can only invade the GDL by a finite depth. In Fig. 4, a fixed water velocity is set at the GDL bottom. In this condition, the liquid water pressure will increase until break through the GDL. Thus, the liquid water saturation in Fig. 4 is different with that in Fig. 2.

It can also be observed that the return of local liquid water saturation at about h = 0.4. This might be due to the local large porosity, as highlighted with box in Fig. 4. We also investigated several perforation depths at the GDL center, and found the perforation at the GDL center has a very small effect on water removal. This is because the GDL center is far away from the liquid water break-through point and little liquid water is present there.

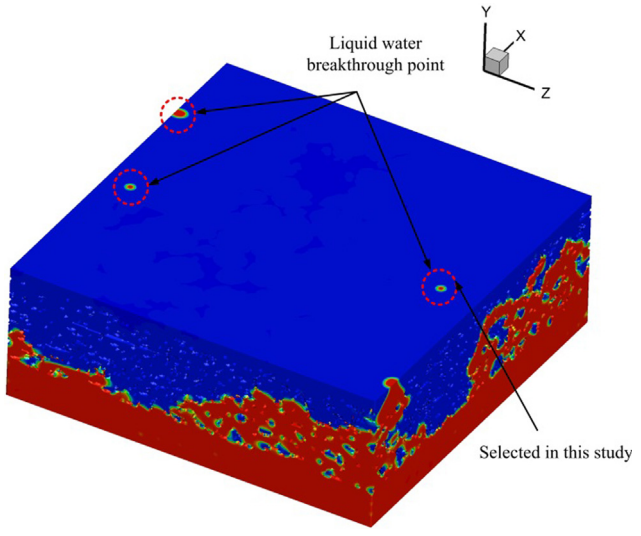

Fig. 3. Liquid water break-through points in the GDL without perforation. The boundary condition at the bottom is constant water velocity.

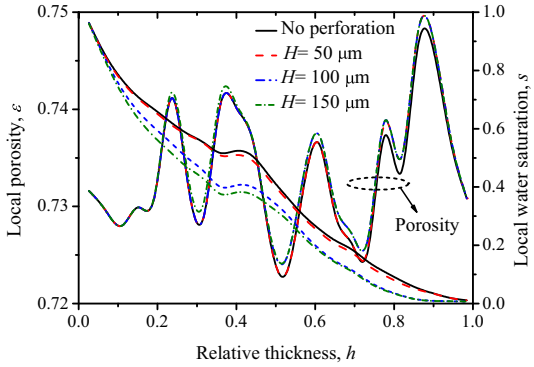

Fig. 4. Local liquid water saturations and porosities in the TP direction of the GDLs with different perforation depths H = 0 μm, 50 μm, 100 μm, 150 μm and D = 50 μm.

Fig. 5 shows the liquid water distributions for different perforation depths H at the planes of X = 500 μm and Z = 700 μm, respectively. These views were obtained at the corresponding cross sections, not average of planes in these two directions. The perforation location is near the break-through point. It is seen that perforation H = 50 μm reduces minor liquid water level the. As the perforation depth increases to 100 μm and 150 μm, the liquid water far away from the perforation can be further reduced.

3.3. Effects of the perforation diameter

In this section, the effects of the perforation diameter D are investigated. The perforation depth H is set as 100 μm. Four diameters of 25 μm, 50 μm, 100 μm and 150 μm are compared with the perforation located at X = 500 μm and Z = 700 μm. The range of the diameter is selected according to the in-situ experiment of Haußmann et al. [28]. Besides, too large perforation may cause side effects, such as inadequate heat removal and membrane support [28]. Fig. 6 shows the local porosities and water saturations in the TP direction for the four perforation diameters. It is seen that the smallest perforation (D = 25 μm) shows a slightly higher liquid saturation than that without perforation near h = 0 and nearly no effects near h = 1. All the other three cases of D = 50 μm, 100 μm, 150 μm significantly decrease the liquid water level, with D = 100 μm showing the lowest liquid saturation. When D changes from 100 μm to 150 μm, the liquid level increases slightly. The observation for D = 25 μm may be due to the fact that the pores in carbon paper can be as large as 20–40 μm [52,58]. As a result, the small perforation, i.e. D = 25 μm, has little change on the GDL's pore structure to promote water break-through. Note that large perforation presents a small resistance to liquid break-through. When the perforation diameter is larger than most of the GDL pores, increasing D will not benefit water removal. Fig. 7 shows the 2D liquid water distributions at the planes of X = 500 μm and Z = 700 μm, respectively. It is seen that as the perforation diameter increases, the more liquid water nearby the perforation is drained by the perforation.

3.4. Effects of the perforation location

In this section, two different perforation locations are studied. The perforation 1 is located at the sample center (i.e. X = 400 μm and Z = 400 μm) and the perforation 2 is near the break-through point at X = 500 μm and Z = 700 μm, as shown in Fig. 8. The perfo-

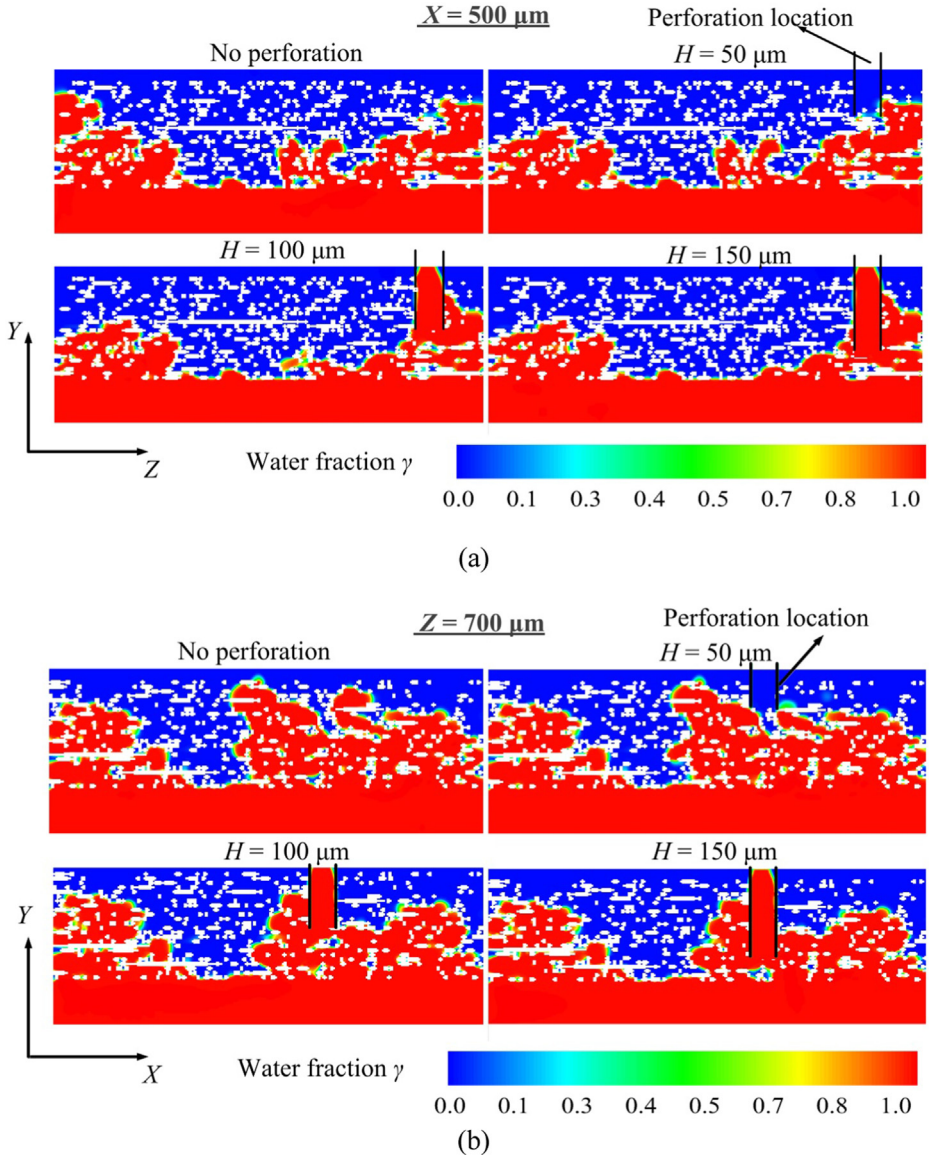

Fig. 5. 2D contours of liquid water fraction at the planes $X = 500$ μm and $Z = 700$ μm in the GDLs with different perforation depths $H = 0$ μm, 50 μm, 100 μm, 150 μm and $D = 50$ μm.

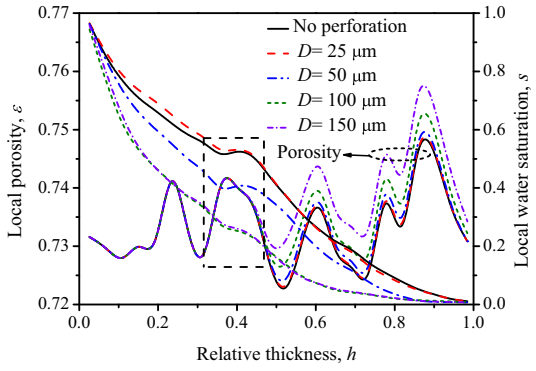

Fig. 6. Local liquid water saturations and porosities in the TP direction of the GDLs with different perforation diameters $D = 0$ μm, 25 μm, 50 μm, 100 μm, 150 μm and $H = 100$ μm.

ration 1 location is chosen far away from the liquid water break-through point to compare with the perforation 2 which is near the break-through point. The diameter and depth of the perforations are set as $D = 50$ μm and $H = 100$ μm, respectively. Fig. 8 shows the local porosities and liquid water saturations in the TP direction for these two perforations. It is seen that the perforation 1 has minor liquid water decrement compared with the perforation 2, which can be explained by Fig. 9: the perforation 1 is not in touch of the liquid water front inside the GDL because it is not near the break-through site. Thus, one can conclude that the perforation location near the liquid water break-through points is preferable to maximize liquid water drainage. Although the perforation 1 doesn't interact with liquid water front in Figs. 8 and 9, it increases the liquid water in the GDL slightly. The reason of this is that the perforation 1 increases the porosity of layer 2 (top), decreasing the entire capillary resistance here. The liquid water is easier to invade into layer 2 and the water accumulation in layer 1 (bottom) is enhanced.

The study shows that using the perforation technique needs to be careful in design. In addition, the liquid water break-through sites can be identified by visualization techniques such as scanning electron microscope (SEM) [59], optical microscope [60] and atomic force microscope [61].

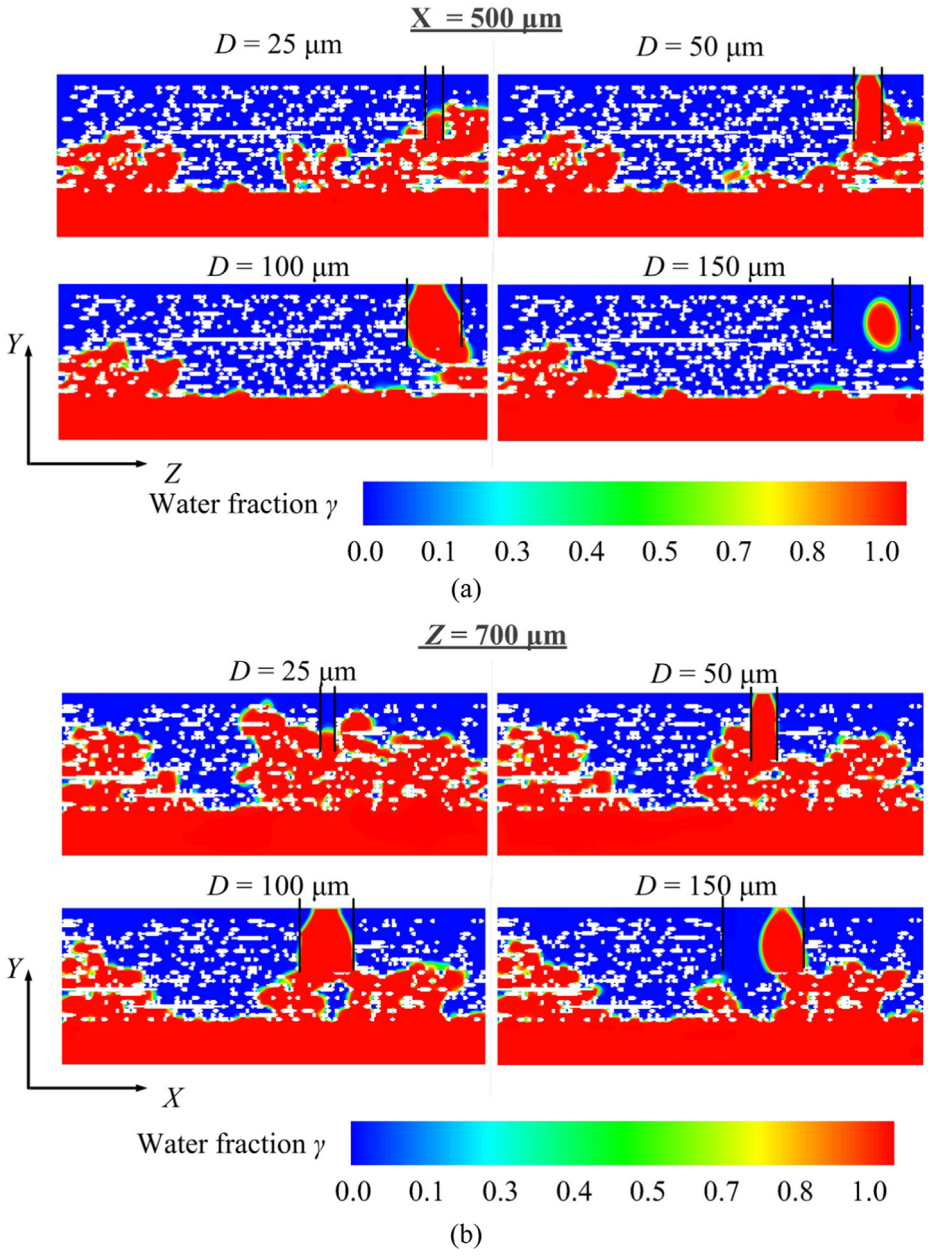

Fig. 7. 2D contours of liquid water fraction at the planes $X = 500$ μm and $Z = 700$ μm, respectively, in the GDLs with different perforation diameters $D = 25$ μm, 50 μm, 100 μm, 150 μm and $H = 100$ μm.

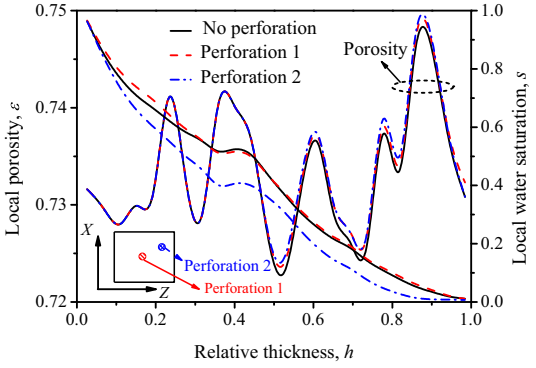

Fig. 8. Local liquid water saturations in the TP direction of the GDL at two perforation locations, respectively (perforation 1 is located at the GDL center and perforation 2 is located at the liquid water break-through point, see Fig. 3).

3.5. Effects of the perforation perimeter wettability

In the laser perforation process, the surface properties of the GDL structure nearby the perforation may be changed due to the oxygenation of carbon fibers in the high temperature. As a result, the local fiber surface becomes hydrophilic [16,17,24]. In this study, a hydrophilic perimeter area is assumed to be a 20 μm width, see Fig. 10, with a contact angle set as $\theta = 80°$. The perforation depth in this section is chosen as $H = 100$ μm. Fig. 10 shows the local liquid water saturations in the TP direction with the hydrophilic and hydrophobic perforation perimeters, respectively (the hydrophobic contact angle $\theta = 109°$). It is seen that the hydrophilic perimeter further reduces the water level in the GDL. This is because the hydrophilic area enlarges the water flow path around the perforation, as shown in Fig. 11.

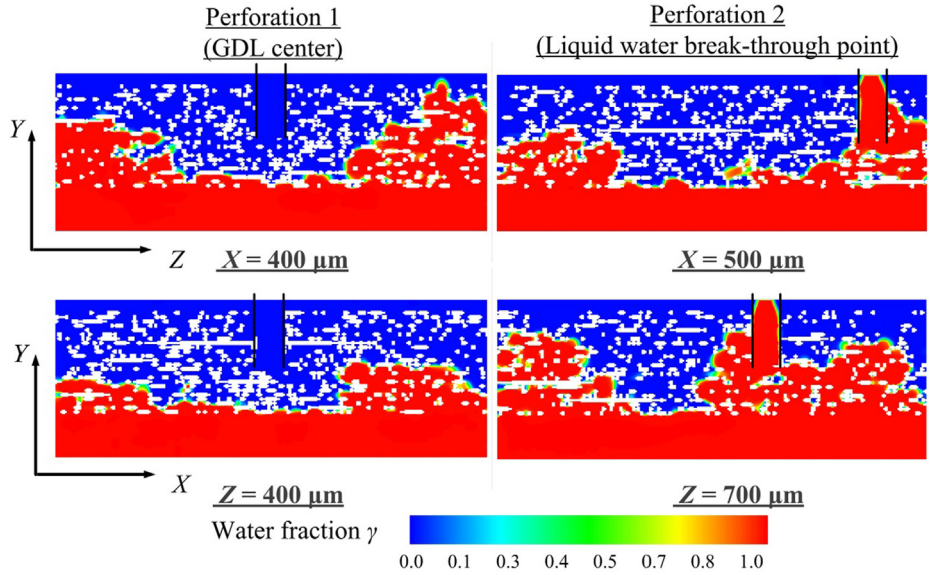

Fig. 9. 2D contours of liquid water fraction at the planes X = 400 μm, 500 μm and Z = 400 μm, Z = 700 μm respectively, in the GDLs with two perforation locations (GDL center and liquid water break-through point).

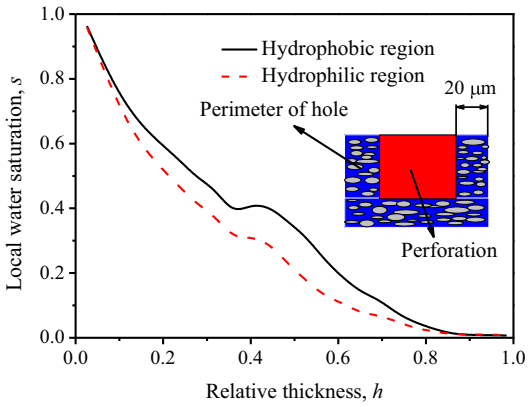

Fig. 10. Local liquid water saturations in the TP direction of the GDLs with a hydrophilic (the contact angle θ = 80°) or hydrophobic (θ = 109°) perforation perimeter (D = 50 μm, H = 100 μm).

3.6. Oxygen transport in partially-saturated GDLs

As well known, the existence of liquid water in GDLs will block oxygen transport. An oxygen diffusion model [47] was employed to investigate the effect of perforation on oxygen transport using the 3D liquid water distribution in Section 3.3. Because of the water injection boundary condition near the GDL bottom, the "water flooding" region near the GDL bottom will severely block the oxygen transport. In this section, the liquid water in the GDL region above the water inlet of ~8 μm thick is removed from the simulation. This thickness responds to the thickness of one fiber layer. The local averaged oxygen concentration C_a in the TP direction for different perforation diameters are shown in Fig. 12. The local averaged oxygen is averaged over the in-plane dimension, not in the entire GDL area. It is seen that a high liquid saturation blocks oxygen diffusion efficiently in all the five cases. Except the case D = 25 μm, the other three perforations considerably reduce the

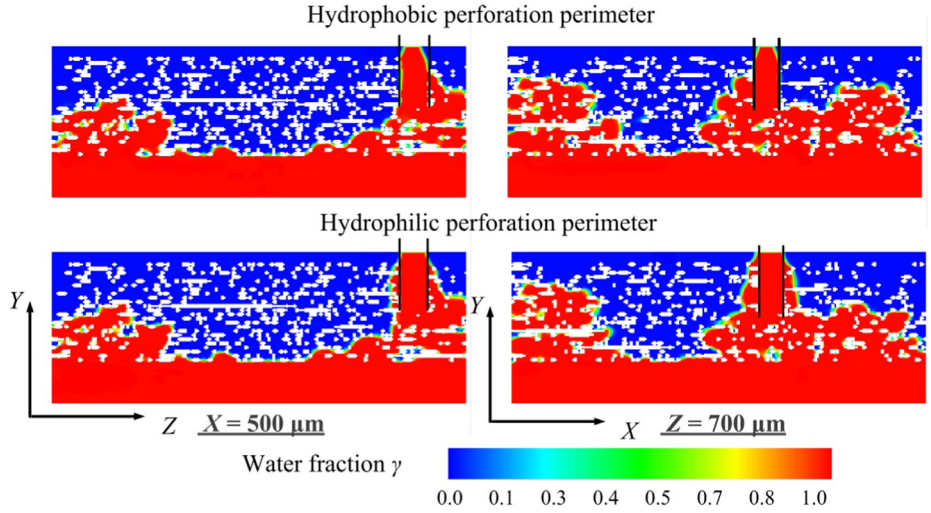

Fig. 11. 2D contours of the liquid water fraction at the planes X = 500 μm and Z = 700 μm, respectively, in the GDLs with a hydrophilic (the contact angle θ = 80°) or hydrophobic (θ = 109°) perforation perimeter.

oxygen transport resistance, as shown by the increased oxygen concentration at the GDL bottom. The case $D = 25$ μm fails to enhance the oxygen concentration is because the slightly higher liquid water saturation in the GDL, which has been discussed in Section 3.3. Fig. 13 shows the 2D oxygen concentration distribution at the plane $Z = 700$ μm in the GDLs with the water distributions shown in Figs. 5 and 7. The averaged oxygen concentrations at the GDL bottom are improved by 14.5%, 101.7% and 76.9% in the three GDLs of $D = 50$ μm, 100 μm and 150 μm, respectively. It is noted that the oxygen concentration increment is more significant when D changes 50 μm to 100 μm than $D = 25$ μm to 50 μm. This is because most pores in the carbon paper is among 20–40 μm [52,58], a small perforation, e.g. 25 μm has little changes on the GDL morphology, thereby reduces the liquid water level slightly. The perforation will take significant effect when its diameter is larger than most pores in the GDL. The averaged liquid water distributions in the in-plane cross-section of perforated GDLs with different perforation diameter are shown in Fig. 14. These liquid water saturations are obtained by averaging the liquid water fraction in the through-plane direction, i.e. y direction. It is seen that more void space is available for oxygen diffusion when $D = 100$ μm than $D = 25$ μm and 50 μm. In summary, the GDL perforation reduces liquid water saturation, thereby decreases the oxygen transport resistance.

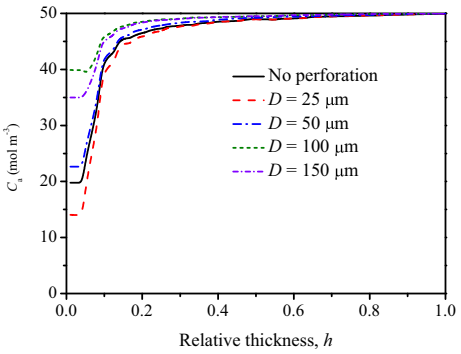

Fig. 12. Local averaged oxygen concentrations in the TP direction of partially-saturated GDLs with different perforation diameters $D = 0$ μm, 25 μm, 50 μm, 100 μm, 150 μm and $H = 100$ μm.

4. Conclusions

In this study, two-phase flow in perforated GDLs was numerically investigated by the two-phase volume of fluid (VOF) model. A stochastic reconstruction method was adopted to reconstruct the GDL microstructures. Various perforation depths and diameters were investigated and compared. The results showed that perforation can considerably reduce the liquid water saturation in the through-plane (TP) direction. The perforation location's dependence was studied. It was found that the GDL perforation should be near the water break-through point to better facilitate liquid water removal. Moreover, it was also found that the perforation perimeter's wettability has pronounced effect on water distribution and that the hydrophilic perimeter further reduces the water saturation in GDLs. Using the predicted water distributions, oxygen diffusion in the perforated GDLs was investigated. It was found that the oxygen transport resistance can be reduced considerably by perforating GDLs. The results of this study show the relationship among the perforation dimensions, liquid water removal, and oxygen supply in the GDL. These findings will improve our understandings of pore-scale liquid water behaviors in the GDL and benefit GDL perforation design for liquid water management.

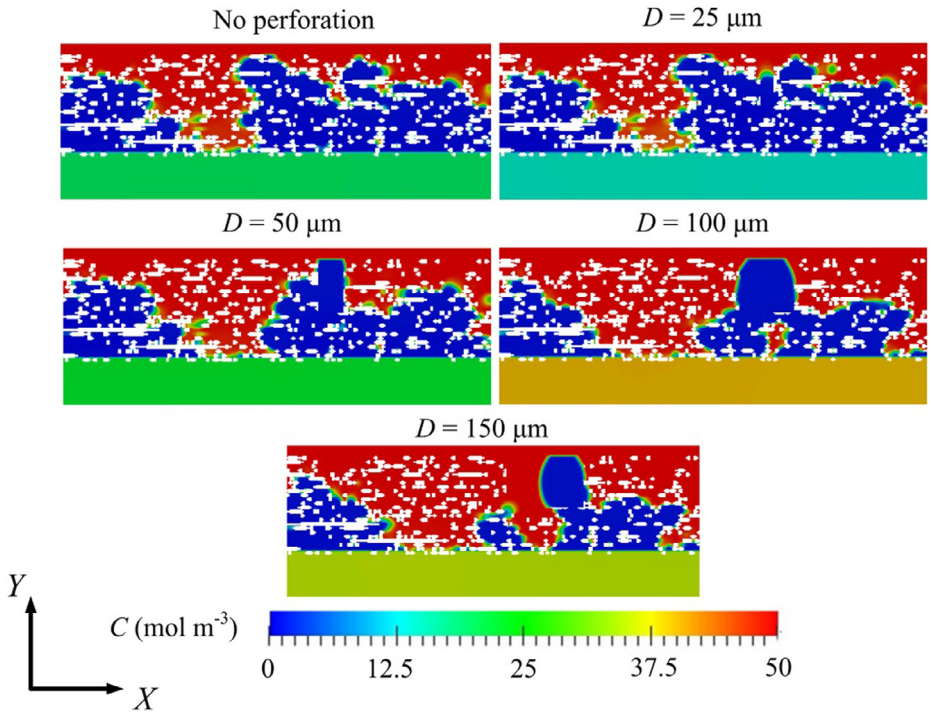

Fig. 13. 2D contours of oxygen concentrations at the slice $Z = 700$ μm in partially-saturated GDLs with different perforation diameters $D = 0$ μm, 25 μm, 50 μm, 100 μm, 150 μm and $H = 100$ μm.

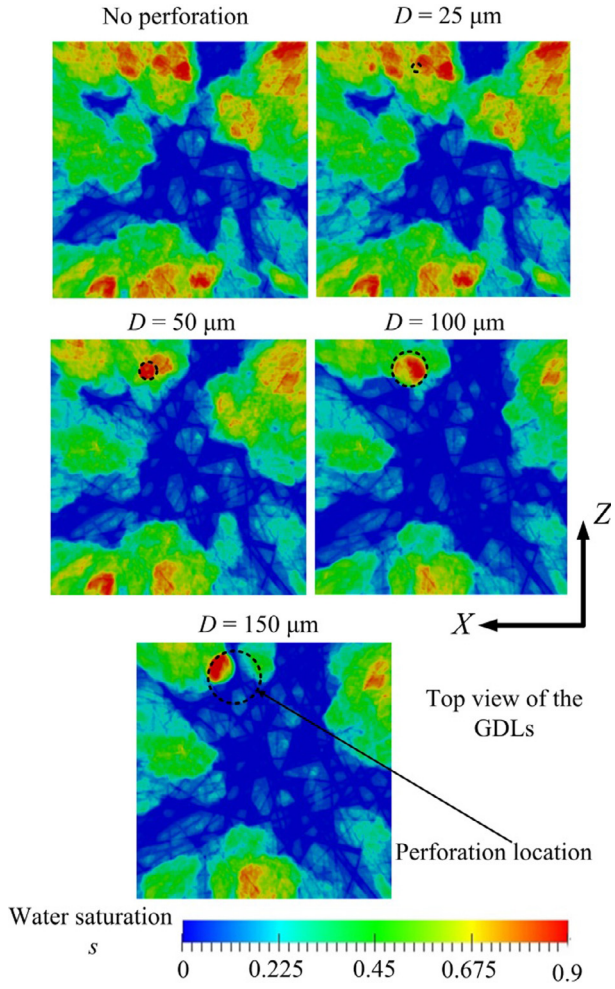

Fig. 14. 2D contours of local average liquid water saturation s in the in-plane cross-section of partially-saturated GDLs with different perforation diameters D = 0 μm, 25 μm, 50 μm, 100 μm, 150 μm and H = 100 μm.

Declaration of Competing Interest

The authors declared that there is no conflict of interest.

Acknowledgement

This work is supported by the National Key Research and Development Program of China (Grant No. 2018YFB0105601) and the National Natural Science Foundation of China for Excellent Young Scholars (Grant No. 51622606). Y. Wang also thanks Shanghai Everpower Technologies Ltd for partial financial support. All the simulations were performed on the Tianhe-HPC1 system at the National Supercomputer Center in Tianjin, China.

References

[1] Y. Wang, K. Chen, J. Mishler, S. Cho, X. Adroher, A review of polymer electrolyte membrane fuel cells: technology, applications, and needs on fundamental research, Appl. Energy 88 (2011) 981–1007.
[2] Y. Luo, K. Jiao, Cold start of proton exchange membrane fuel cell, Progr. Combust. Sci. 64 (2018) 29–61.
[3] Y. Wang, K. Chen, PEM Fuel Cells: Thermal and Water Management Fundamentals, Momentum Press, 2013.
[4] K. Jiao, X. Li, Water transport in polymer electrolyte membrane fuel cells, Prog. Energy Combust. Sci. 37 (2011) 221–291.
[5] M. Mathias, J. Roth, J. Fleming, W. Lehnert, Diffusion media materials and characterization, in: W. Lietsich, A. Lamm, H.A. Gasteiger (Eds.), Handbook of Fuel Cells-Fundamentals, Technology and Applications, Wiley, 2003.
[6] Y. Wang, S. Cho, R. Thiedmann, V. Schmidt, W. Lehnert, X. Feng, Stochastic modeling and direct simulation of the diffusion media for polymer electrolyte fuel cells, Int. J. Heat Mass Transfer 53 (2010) 1128–1138.
[7] X. Xie, R. Wang, K. Jiao, G. Zhang, J. Zhou, Q. Du, Investigation of the effect of micro-porous layer on PEM fuel cell cold start operation, Renewable Energy 117 (2018) 125–134.
[8] G. Chen, G. Zhang, L. Guo, H. Liu, Systematic study on the functions and mechanisms of micro porous layer on water transport in proton exchange membrane fuel cells, Int. J. Hydrogen Energy 41 (2016) 5063–5073.
[9] J. Shan, R. Lin, X. Chen, X. Diao, EIS and local resolved current density distribution analysis on effects of MPL on PEMFC performance at varied humidification, Int. J. Heat Mass Transfer 127 (2018) 1076–1083.
[10] J. Lee, J. Hinebaugh, A. Bazylak, Synchrotron X-ray radiographic investigations of liquid water transport behavior in a PEMFC with MPL-coated GDLs, J. Power Sources 227 (2013) 123–130.
[11] S. Shimpalee, V. Lilavivat, H. Xu, C. Mittelsteadt, Y. Khunatorn, Experimental investigation and numerical determination of custom gas diffusion layers on PEMFC performance, Electrochim. Acta 222 (2016) 1210–1219.
[12] G. Park, Y. Sohn, T. Yang, Y. Yoon, W. Lee, C. Kim, Effect of PTFE contents in the gas diffusion media on the performance of PEMFC, J. Power Sources 131 (2004) 182–187.
[13] L. Giorgi, E. Antolini, A. Pozio, E. Passalacqua, Influence of the PTFE content in the diffusion layer of low-Pt loading electrodes for polymer electrolyte fuel cells, Electrochim. Acta 43 (1998) 3675–3680.
[14] P. Yi, L. Peng, X. Lai, M. Li, J. Ni, Investigation of sintered stainless steel fiber felt as gas diffusion layer in proton exchange membrane fuel cells, Int. J. Hydrogen Energy 37 (2012) 11334–11344.
[15] H. Choi, O. Kim, M. Kim, H. Choe, Y. Cho, Y. Sung, Next-generation polymer-electrolyte-membrane fuel cells using titanium foam as gas diffusion layer, ACS Appl. Mater. Interfaces 6 (2014) 7665–7671.
[16] D. Gerteisen, T. Heilmann, C. Ziegler, Enhancing liquid water transport by laser perforation of a GDL in a PEM fuel cell, J. Power Sources 177 (2008) 348–354.
[17] D. Gerteisen, C. Sadeler, Stability and performance improvement of a polymer electrolyte membrane fuel cell stack by a laser perforation of gas diffusion layers, J. Power Sources 195 (2010) 5252–5257.
[18] M. Manahan, M. Mench, Laser perforated fuel cell diffusion media: engineered interfaces for improved ionic and oxygen transport, J. Electrochem. Soc. 159 (7) (2012) F322–F330.
[19] M. Manahan, J. Clement, A. Srouji, S. Brown, T. Reutzel, M. Mench, Laser modified fuel cell diffusion media: engineering enhanced performance via localized water redistribution, J. Electrochem. Soc. 161 (10) (2014) F1061–F1069.
[20] M. Manahan, M. Hatzell, E. Kumnur, M. Mench, Laser perforated fuel cell diffusion media. Part I: Related changes in performance and water content, J. Power Sources 196 (13) (2011) 5573–5582.
[21] J. Lu, J. Waldecker, X. Xie, M. Lai, D. Hussey, D. Jacobson, Investigation of water transport in perforated gas diffusion layer by neutron radiography, ECS Trans. 58 (1) (2013) 315–324.
[22] N. Cooper, A. Santamaria, M. Becton, J. Park, Neutron radiography measurements of in-situ PEMFC liquid water saturation in 2D&3D morphology gas diffusion layers, Int. J. Hydrogen Energy 42 (2017) 16269–16278.
[23] A. Iranzo, P. Boillat, F. Rosca, Validation of a three dimensional PEM fuel cell CFD model using local liquid water distributions measured with neutron imaging, Int. J. Hydrogen Energy 39 (2014) 7089–7099.
[24] R. Alink, D. Gerteisen, W. Merida, Investigation the water transport in porous media for PEMFCs by liquid water visualization in ESEM, Fuel Cells 11 (2011) 481–488.
[25] J. Nam, K. Lee, G. Hwang, C. Kim, M. Kaviany, Microporous layer for water morphology control in PEMFC, Int. J. Heat Mass Transfer 52 (2009) 2779–2791.
[26] H. Markotter, R. Alink, J. Haußmann, K. Dittmann, T. Arlt, F. Wieder, C. Totzke, M. Klages, C. Reiter, H. Riesemeier, J. Scholta, D. Gerteisen, J. Banhart, I. Manke, Visualization of the water distribution in perforated gas diffusion layers by means of synchrotron X-ray radiography, Int. J. Hydrogen Energy 37 (2012) 7757–7761.
[27] R. Alink, J. Haußmann, H. Markotter, M. Schwager, I. Manke, D. Gerteisen, The influence of porous transport layer modifications on the water management in polymer electrolyte membrane fuel cells, J. Power Sources 233 (2013) 358–368.
[28] J. Haußmann, H. Markotter, R. Alink, A. Bauder, K. Dittmann, I. Manke, J. Scholta, Synchrotron radiography and tomography of water transport in perforated gas diffusion media, J. Power Sources 239 (2013) 611–622.
[29] I. Zenyuk, D. Parkinson, G. Hwang, A. Weber, Probing water distribution in compressed fuel-cell gas-diffusion layers using X-ray computed tomography, Electrochem. Commun. 53 (2015) 24–28.
[30] D. Muirhead, R. Banerjee, M. George, N. Ge, P. Shrestha, H. Liu, J. Lee, A. Bazylak, Liquid water saturation and oxygen transport resistance in polymer electrolyte membrane fuel cell gas diffusion layers, Electrochim. Acta 274 (2018) 250–265.
[31] Y. Wang, K. Chen, Through-plane water distribution in a polymer electrolyte fuel cell: comparison of numerical prediction with neutron radiography data, J. Electrochem. Soc. 157 (2010) B1879–B1886.
[32] Y. Wang, K. Chen, Effect of spatially-varying GDL properties and land compression on water distribution in PEM fuel cells, J. Electrochem. Soc. 158 (2011) B1292–B1299.
[33] J. Baschuk, X. Li, A general formulation for a mathematical PEM fuel cell model, J. Power Sources 142 (2005) 134–153.

[34] N. Zamel, X. Li, A parametric study of multi-phase and multi-species transport in the cathode of PEM fuel cells, Int. J. Energy Research 32 (2008) 698–721.
[35] Y. Wang, Modeling of two-phase transport in the diffusion media of polymer electrolyte fuel cells, J. Power Sources 185 (2008) 261–271.
[36] W. Fang, Y. Tang, L. Chen, Q. Kang, W. Tao, Influences of the perforation on effective transport properties of gas diffusion layers, Int. J. Heat Mass Transfer 126 (2018) 243–255.
[37] L. Chen, H. Luan, Y. He, W. Tao, Pore-scale flow and mass transport in gas diffusion layer of proton exchange membrane fuel cell with interdigitated flow fields, Int. J. Therm. Sci. 51 (2012) 132–144.
[38] G. Molaeimanesh, M. Akbari, Impact of PTFE distribution on the removal of liquid water from a PEMFC electrode by lattice Boltzmann method, Int. J. Hydrogen Energy 39 (2014) 8401–8409.
[39] W. Chen, F. Jiang, Impact of PTFE content and distribution on liquid–gas flow in PEMFC carbon paper gas distribution layer: 3D lattice Boltzmann simulations, Int. J. Hydrogen Energy 41 (2016) 8550–8562.
[40] S. Kuttanikkad, M. Prat, J. Pauchet, Pore-network simulations of two-phase flow in a thin porous layer of mixed wettability: application to water transport in gas diffusion layers of proton exchange membrane fuel cells, J. Power Sources 196 (2011) 1145–1155.
[41] M. Shahraeeni, M. Hoorfar, Pore-network modeling of liquid water flow in gas diffusion layers of proton exchange membrane fuel cells, Int. J. Hydrogen Energy 39 (2014) 10697–10709.
[42] P. Carrere, M. Prat, Liquid water in cathode gas diffusion layers of PEM fuel cells: Identification of various pore filling regimes from pore network simulations, Int. J. Heat Mass Transfer 129 (2019) 1043–1056.
[43] J. Park, K. Jiao, X. Li, Numerical investigations on liquid water removal from the porous gas diffusion layer by reactant flow, Appl. Energy 87 (2010) 2180–2186.
[44] Y. Yin, T. Wu, P. He, Q. Du, K. Jiao, Numerical simulation of two-phase cross flow in microstructure of gas diffusion layer with variable contact angle, Int. J. Hydrogen Energy 39 (2014) 15772–15785.
[45] Z. Niu, K. Jiao, Y. Wang, Q. Du, Y. Yin, Numerical simulation of two-phase cross flow in the gas diffusion layer microstructure of proton exchange membrane fuel cells, Int. J. Energy Research 42 (2018) 802–816.
[46] Z. Niu, Y. Wang, K. Jiao, J. Wu, Two-Phase flow dynamics in the gas diffusion layer of proton exchange membrane fuel cells: volume of fluid modeling and comparison with experiment, J. Electrochem. Soc. 165 (9) (2018) F613–F620.
[47] Z. Niu, J. Wu, Y. Wang, K. Jiao, Investigating the in-/through-plane effective diffusivities of dry and partially-saturated gas diffusion layers, J. Electrochem. Soc. 165 (11) (2018) F1–F8.
[48] Z. Niu, Z. Bao, J. Wu, Y. Wang, J. Kui, Two-phase flow in the mixed-wettability gas diffusion layer of proton exchange membrane fuel cells, Appl. Energy 232 (2018) 443–450.
[49] A. Bazylak, D. Sinton, Z. Liu, N. Djilali, Effect of compression on liquid water transport and microstructure of PEMFC gas diffusion layers, J. Power Sources 163 (2007) 784–792.
[50] R. Fluckiger, F. Marone, M. Stampanoni, A. Wokaun, F. Buchi, Investigation of liquid water in gas diffusion layers of polymer electrolyte fuel cells using X-ray tomographic microscopy, Electrochim. Acta 56 (2011) 2254–2262.
[51] C. Hartnig, I. Manke, R. Kuhn, S. Kleinau, J. Goebbels, J. Banhart, High-resolution in-plane investigation of the water evolution and transport in PEM fuel cells, J. Power Sources 188 (2009) 468–474.
[52] Y. Wang, K. Chen, S. Cho, PEM Fuel Cells: Thermal and Water Management Fundamentals, Momentum Press, 2013.
[53] S. Sakaida, Y. Tabe, T. Chikahisa, Large scale simulation of liquid water transport in a gas diffusion layer of polymer electrolyte membrane fuel cells using the lattice Boltzmann method, J. Power Sources 361 (2017) 133–143.
[54] P. Satjaritanun, S. Hirano, A. Shum, I Zenyuk, A weber. Fundamental understanding of water movement in gas diffusion layer under different arrangements using combination of direct modeling and experimental visualization, J. Electrochem. Soc. 165 (2018) F1115–F1126.
[55] L. Hao, P. Cheng, Lattice Boltzmann simulations of water transport in gas diffusion layer of a polymer electrolyte membrane fuel cell, J. Power Sources 195 (2010) 3870–3881.
[56] L. Hao, P. Cheng, Capillary pressures in carbon paper gas diffusion layers having hydrophilic and hydrophobic pores, Int. J. Heat Mass Transfer 55 (2012) 133–139.
[57] J. Fairweather, P. Cheung, J. St-Pierre, D. Schwartz, A microfluidic approach for measuring capillary pressure in PEMFC gas diffusion layers, Electrochem. Commun. 9 (2007) 2340–2345.
[58] S. Simaafrookhteh, M. Shakeri, M. Baniassadi, A. Sahraei, Microstructure reconstruction and characterization of the porous GDLs for PEMFC based on fibers orientation distribution, Fuel Cells 28 (2018) 160–172.
[59] S. Huang, P. Ganesan, H. Jung, B. Popov, Development of supported bifunctional oxygen electrocatalysts and corrosion-resistant gas diffusion layer for unitized regenerative fuel cell applications, J. Power Sources 198 (2012) 23–29, https://doi.org/10.1016/j.jpowsour.2011.09.071.
[60] S. Lister, D. Sinton, N. Djilali, Ex situ visualization of liquid water transport in PEM fuel cell gas diffusion layers, J. Power Sources 154 (2006) 95–105.
[61] S. Botelho, A. Bazylak, Impact of polymer electrolyte membrane fuel cell microporous layer nano-scale features on thermal conductance, J. Power Sources 280 (2015) 173–181.